IEEE Access
Multidisciplinary | Rapid Review | Open Access Journal

Received 21 February 2022, accepted 26 March 2022, date of publication 31 March 2022, date of current version 3 August 2022.

Digital Object Identifier 10.1109/ACCESS.2022.3163726

APPLIED RESEARCH

Research on Surface Defect Detection Technology Based on the Zonal and Time-Sharing Computational Imaging

CHEN LI[1,2], YONGJING YIN[1], BIN YUAN[1], AND XIANGQING LI[2]

[1]School of Mechanical and Energy Engineering, Zhejiang University of Science and Technology, Hangzhou 310023, China
[2]School of Engineering, Westlake University, Hangzhou 310024, China

Corresponding authors: Yongjing Yin (yyj7766@126.com) and Xiangqing Li (lixiangqing@westlake.edu.cn)

This work was supported in part by the Zhejiang Provincial Natural Science Foundation of China under Grant LGF20F050002, in part by the National Natural Science Foundation of China under Grant 62103340, and in part by the Independent Application Project of Agricultural and Social Development Scientific Research in Hangzhou under Grant 20191203B34.

ABSTRACT In order to solve the misjudgment problem of different information in common gray images due to the very similar features such as morphology and gray value, and to avoid the high cost of using the 3-D sensor in defect detection, a zonal and time-sharing computational imaging (ZTSCI) is proposed in this paper. Firstly, a four-zone and time-sharing exposure visual imaging system is constructed by monocular telecentric imaging and lights in different directions. Then, according to the gray images under four groups of illumination conditions, and the direction vectors of incident lights, five feature images are calculated, such as fused images of maximum and average, enhanced images of normal vector, gradient and relative height. On the one hand, the image background fluctuation caused by the calculation error introduced by the ideal hypothesis is weakened, and the interference of surface texture to defect detection is reduced. On the other hand, the difference of easily-confused information can be increased in different feature spaces. In this paper, the ZTSCI is further applied to defect detection on the surface of new energy batteries. It solves the problem that defects and interference information are difficult to distinguish in gray images captured with common machine vision methods, reduces the difficulty of subsequent defect recognition, and lays a foundation for improving the accuracy of recognition.

INDEX TERMS Defect detection, machine vision, zonal lighting, feature enhancement.

I. INTRODUCTION

In recent years, the surface defect detection technology based on two-dimensional machine vision has been rapidly applied and developed. Through specific imaging methods (bright field, dark field, etc.) [1]–[4], the information to be detected is stored in the image with the characteristics of brightness variation. Furthermore, image preprocessing techniques (filtering, texture enhancement, etc.) are used to eliminate the interference information and extract the defect information [5]–[11]. Alternatively, deep learning can be used to achieve segmentation and recognition of the defects based on gray images [12]–[16]. However, in most industrial field inspection, it still relies on manual visual inspection. The main reason is that the human eyes can observe the surface from different angles, so that it can obtain more forms of information. However, common machine vision detection methods can only get the characteristics of brightness variation in the gray images, and only get the image information from a single perspective in most cases. So, it cannot get the defect information in different feature spaces, and it is easy to misjudge some defects and interference information (non-defect). For example, in the common defect detection of new energy battery surface, interference information may occur, causing the detection device to fail to meet the requirements of the site. The surface to be detected will exist pit defects and foreign material raised on the surface, scratch defects and some bright lines without damaging the functionality of the surface. The above information has similar characteristics of morphology and grayscale variation. Thus, it is easy to generate misjudgment in the gray image, as shown in Fig. 1.

Pits in (a1) and (b2) are produced when sharp objects destroy the surface during production, and foreign material in (b1) refers to non-defect attached to the surface by external

The associate editor coordinating the review of this manuscript and approving it for publication was Oguzhan Urhan.

dirt. Shallow marks in (c1) are mainly caused by sharp objects across the surface slightly, only damaging the surface coating. And it is too shallow to be considered defects because it does not damage the functionality of product, which referred to simply as non-functional defect. And scratches in (d1) and (d2) are the common defects damaging the surface quality, which should be detected. However, the brightness variation of them is very similar in the gray image, so it is easy to produce misjudgment when detection.

Based on the above problems, machine learning in [17]–[20] can extract different features based on grayscale images, which can increase the accuracy of recognition to a certain extent. However, it cannot get good effect in the above application because of the similarity of morphology and grayscale variation. In addition, 3D-vision in [21]–[24], polarization in [25], [26], total internal reflection in [27] and other means can also be used to identify defects. For example, the height of defects can be achieved by 3D-vision, which can be used to distinguish raised features from sunken features. However, this method has a large amount of data and high detection cost, so it is difficult to be applied in the industrial field. In view of the above problems, it's found in the study that when the lights incident from different angles, there will be some differences for the raised and sunken features. That is, the shadow feature changes with different light angles. Further, the characteristics of surface gradient and height can be obtained by using shadow analysis in [28], [29] or photometric stereo in [30]–[32]. The photometric stereo is based on the ideal theoretical assumptions [33], [34]: (1) the light sources are at infinity; (2) the surface is a Lambert reflector; (3) the camera imaging model is orthogonal model. However, this technology is often difficult to meet the above conditions in practical application, resulting in a large difference between the calculated results and the actual surface characteristics.

Based on the analysis of the above problems, a zonal and time-sharing computational imaging (ZTSCI) is proposed in this paper, according to the characteristics of different shadows produced by different lighting angles, combined with photometric stereo and image processing technology. For ZTSCI, the shadow features generated under different incident lights are saved in the images through monocular vision, using a four-zone and time-sharing exposure visual imaging system. Then, the gradient information of the surface is reconstructed through the grayscale variation and the direction of the lights. The surface reconstruction theory, image preprocessing and enhancement technology are also combined to enhance the information that can characterize height changes, while weakening the complex texture on the surface. In addition, it can avoid large surface fluctuation error caused by theoretical hypothesis in practical calculation. Furthermore, the ZTSCI proposed in this paper is used to complete feature enhancement on new energy battery surface. On the one hand, it overcomes the limitations of traditional photometric stereo in industrial applications. On the other hand, it can obtain more features at a lower cost, and increase the difference of some information with similar gray scale feature. In this way, the interference of foreign material and non-functional defect to defect recognition can be avoided. And even the misjudgment caused by the inherent texture of the surface in the later defect recognition can be reduced. The subsequent identification of defects is not described in this paper. The ZTSCI proposed in this paper is mainly applied in the feature enhancement, which increases the separability of confusable information and reduces the difficulty of subsequent defect identification, thus increasing the robustness of detection equipment in practical application.

II. A FOUR-ZONE AND TIME-SHARING EXPOSURE VISUAL IMAGING SYSTEM

In ZTSCI proposed in this paper, incident lights from different angles are irradiated to the surface, and multiple features are calculated according to gray images under different lighting conditions and the direction vectors of incident lights. Firstly, the imaging system is constructed. That is, the images of the surface under different lightings, can be obtained through time-sharing scintillation of four-zone lights, and time-sharing exposure for monocular visual imaging. Further, according to the above images and the angle matrix of lights, the normal vector of the surface is calculated. Based on the normal vector, it is convenient for further surface reconstruction and image preprocessing. The system is mainly composed of monocular telecentric imaging unit and four groups of uniform LED strip lights in different directions, which is shown in Fig. 2.

As shown in Fig. 2, four groups of LED strip lights are evenly distributed at $0°, 90°, 180°, 270°$ horizontally. In order to simulate the uniform light generated by the infinite point light, and ensure that the whole surface can be irradiated, diffusing panels are set at the front of the lights. In addition, in order to simulate the orthogonal imaging model, the system adopts a telecentric optical path, which makes the imaging system only accept the light within a small angle with the main optical axis, so as to enhance the contrast of defects to a certain extent. Moreover, the center of the imaging system is approximately the same as the center of the lights by mechanical means. This makes it easier to distribute the light source more symmetrically around the sample to be tested in the later practical application. Furthermore, dark-field lighting with low-angle is adopted in this paper to form a high contrast between the bright features at the defect location and the dark features in the background, so as to ensure that all defects can be saved in the image. Through the design of the above hardware system, the images containing defects with high contrast can be obtained while ensuring uniform illumination of the surface. Furthermore, the light intensity distributions of the surface under four different incident lights are obtained by using the time-sharing flashing of four groups of uniform LED strip lights, combined with the camera synchronous four times time-sharing exposure. In the subsequent calculation, the normal vector of the surface is solved according to the illumination direction matrix and

the approximate reflection model of the surface. Then, the gradient and height variation of the surface can be calculated, and the defects can be enhanced with the image processing. Besides, the inherent texture characteristics of the surface can be weakened during the calculation.

III. PRINCIPLE OF ZONAL AND TIME-SHARING COMPUTATIONAL IMAGING

Based on the above four-zone and time-sharing exposure visual imaging system, four different sets of shadow distribution can be obtained under four groups of different incident lights. And then, the maximum and average values of the acquired images are fused respectively. In addition, the normal vector can be calculated according to the direction vectors of lights and the approximate reflection model of the surface. Furthermore, the least squares method and image preprocessing techniques are used to obtain the gradient and relative height features of the surface. With the use of ZTSCI, it can avoid the over-large surface shape fluctuation generated in the approximate calculation. Also, it can enhance the defect features, while suppressing the inherent surface texture features. The calculation is shown in Fig. 3.

As shown from the Fig. 3, the fusion of different images is completed by calculating the maximum value and the mean value. Although defects and interference information with similar morphology and gray value cannot be distinguished, defects in the grayscale images above, still have high spatial resolution and strong contrast. Then, the reflectance distribution and normal vector distribution of the surface are calculated by the least square method, combining with the incident vectors of different lights and the surface reflective properties of approximately lambert surface. Furthermore, the normal vector is transformed into color map with strong contrast by using enhancement in different channels, and the local features with large variation are enhanced. In addition, based on the normal vector, the gradient distribution of the surface is calculated. And logarithm transformation, Fourier transformation and filtering operation are used to enhance the defects features with large gradient changes, and weaken the surface shape fluctuation introduced by the theoretical hypothesis. Moreover, the overdetermined linear equations of surface normal vector and tangent plane are established, and the height characteristic is calculated by the least square method. Similarly, the filtering operation is used to reduce the surface shape fluctuation in the absolute height characteristic. And the relatively accurate characteristics of relative height at the defect location are obtained.

It should be noted that the ZTSCI as shown in Fig. 3 is mainly based on the traditional photometric stereo to calculate the light directions and reconstruct the surface topography. However, according to the conditions of the application scene and the design of the visual imaging system, the whole detection system does not meet the assumed conditions of photometric stereo. That is, although the lights are homogenized, it still cannot meet the theoretical hypothesis model of infinite distance. And in practical application, the surface to be detected cannot meet the ideal Lambert model. In addition, although telecentric optical path is used in the design, the imaging still has a certain divergence angle, which cannot meet the ideal orthogonal imaging model. Thus, the above problems can produce a large error in different feature space, such as the surface shape fluctuation mentioned above. In order to avoid the above problems, this paper introduces further filtering into the features calculation, so as to avoid the interference of the excessive fluctuation of the surface topography on the defect detection. The main calculation process is as follows.

Firstly, the lights in the detection system are approximated to uniform lights incident at infinity, and the imaging system is approximated to orthogonal imaging model. The smooth chrome sphere is used to complete the calibration of the direction matrix of the incident lights:

$$\begin{aligned} \boldsymbol{R}+\boldsymbol{L} &= \boldsymbol{N_L} = 2\boldsymbol{S} \\ \boldsymbol{S} &= \frac{(\boldsymbol{R}\cdot\boldsymbol{N})}{|\boldsymbol{N_L}|^2}\boldsymbol{N_L} = (\boldsymbol{R}\cdot\boldsymbol{N_L})\boldsymbol{N_L} \\ \boldsymbol{L} &= 2(\boldsymbol{R}\cdot\boldsymbol{N_L})\boldsymbol{N_L} - \boldsymbol{R} \\ \boldsymbol{N_L} &= (P_x - C_x, P_y - C_y, \sqrt{\boldsymbol{R}^2 - \left[(P_x-C_x)^2+(P_y-C_y)^2\right]}) \end{aligned} \tag{1}$$

where, $\boldsymbol{S}$ is the projection of $\boldsymbol{R}$ on $\boldsymbol{N_L}$, $\boldsymbol{L}$ is the orientation matrix of the four lights, (P_x, P_y) is the imaging center point of the light reflected by the smooth sphere, (C_x, C_y) is the center point of the sphere in the image, $\boldsymbol{R}$ is the unit vector ($[0, 0, 1]$, according to the orthogonal imaging) of the reflected light, and $\boldsymbol{N_L}$ is the unit normal vector at the position of the center point of the reflected light on the smooth sphere.

Then, in order to compare the characteristics of common grayscale images, the four images (Img1,Img2,Img3,Img4) are fused according to (2) and (3). In addition, the gray images after fusion have high spatial resolution and image contrast, and gray features can be used into the later defect recognition.

$$I_{result1} = \max(pixel_1, pixel_2, pixel_3, pixel_4) \tag{2}$$

$$I_{result2} = (pixel_1 + pixel_2 + pixel_3 + pixel_4)/4 \tag{3}$$

where, $I_{result1}, I_{result2}$ represent the image fusion results of maximum and average respectively, calculated point by point. And $pixel_1, pixel_2, pixel_3, pixel_4$ represent the pixel gray values at the corresponding position in the four images.

In addition, the surface to be detected is approximated to the Lambert reflection model, so that:

$$\boldsymbol{I} = r\boldsymbol{N}\cdot\boldsymbol{L} \tag{4}$$

According to the four images captured by visual imaging system, the following equation set can be obtained:

$$\begin{cases} I_1 = r(N_x\cdot L_{1,x} + N_y\cdot L_{1,y} + N_z\cdot L_{1,z}) \\ I_2 = r(N_x\cdot L_{2,x} + N_y\cdot L_{2,y} + N_z\cdot L_{2,z}) \\ I_3 = r(N_x\cdot L_{3,x} + N_y\cdot L_{3,y} + N_z\cdot L_{3,z}) \\ I_4 = r(N_x\cdot L_{4,x} + N_y\cdot L_{4,y} + N_z\cdot L_{4,z}) \end{cases} \tag{5}$$

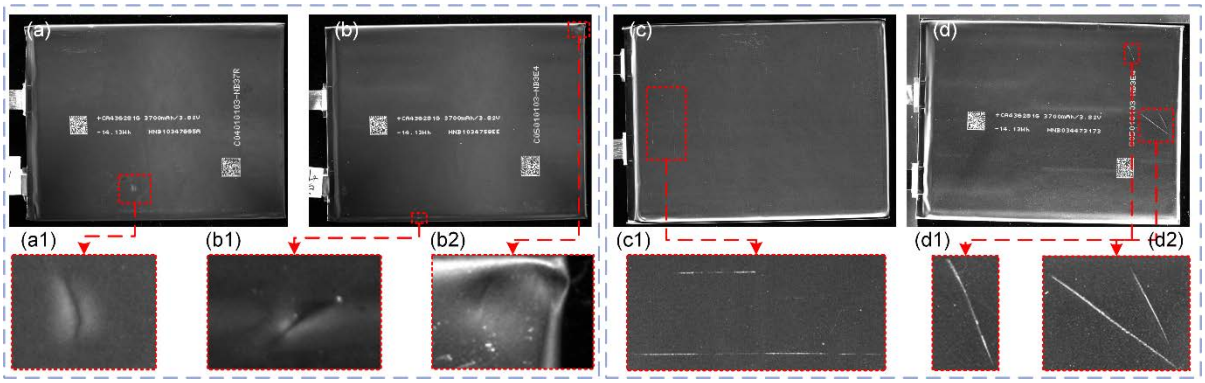

FIGURE 1. Different information of defect detection on new energy battery surface. (a) pit defect in (a1); (b) raised foreign material in (b1), and pit defect in (b2); (c) bright lines or shallow marks in (c1), which don't damage the functionality of product; (d) scratch defects in (d1) and (d2).

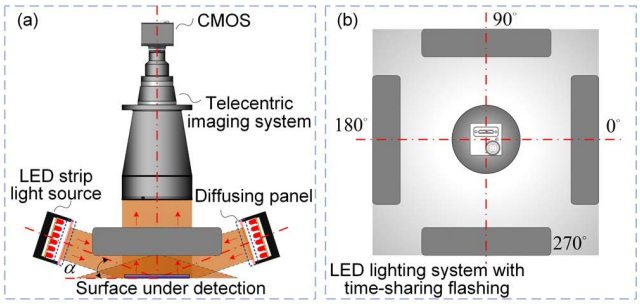

FIGURE 2. Schematic diagram of system structure: (a) the front view of system structure; (b) the top view of system structure.

Further, the least square method is used to solve the above equations:

$$r = \left\| (\boldsymbol{L}^T\boldsymbol{L})^{-1}\boldsymbol{L}^T\boldsymbol{I} \right\|, \quad \boldsymbol{N} = [(\boldsymbol{L}^T\boldsymbol{L})^{-1}\boldsymbol{L}^T\boldsymbol{I}]/r \tag{6}$$

where, $\boldsymbol{I} = (I_1, I_2, I_3, I_4)$ are the imaging results under four groups of illumination, $\boldsymbol{N}$ is the normal vector, and r is the reflectivity. $\boldsymbol{I}, \boldsymbol{L}, \boldsymbol{N}$ have all been normalized.

After obtained the surface normal vector, the three-dimensional data in the normal vector are transformed into color images in this paper. That is, curvature characteristics of the surface changing along different directions are represented by different colors of R, G and B. And, a strong contrast can be obtained by comparing changes in different directions with differentiated color components.

$$I_{result3,ch} = [N_i - \min(N_i)]/[\max(N_i) - \min(N_i)] \tag{7}$$

where, $I_{result3}$ is the 3-channel color image obtained by the above calculation, $ch = 1, 2, 3$, and $N_i \in \{N_x, N_y, N_z\}$.

Further, according to the normal vector $\boldsymbol{N}$, the gradient distribution characteristic $I_g(x, y)$ can be obtained:

$$\begin{cases} p = \partial z/\partial x = -N_x/N_z \\ q = \partial z/\partial y = -N_y/N_z \end{cases} \tag{8}$$

$$\begin{aligned} g(x, y) &= \sqrt{p^2(x, y) + q^2(x, y)} \\ I_g(x, y) &= [g(x, y) - g_{\min}]/(g_{\max} - g_{\min}) \end{aligned} \tag{9}$$

It is noted that some theoretical assumptions are made in the above calculation, such as the uniform illumination at infinity, approximate orthogonal imaging, and approximate lambert surface. However, it will produce the fluctuation of local surface in the gradient characteristic. In order to solve this problem, some filtering operations are introduced to enhance the gradient characteristic of defects and weaken the background. Noted that the gradient fluctuation at the defect location is sharper, this paper adopts logarithm transform and the Fourier transform to separate the background:

$$DFT[\ln(I_g)] = DFT[\ln(I_{obj})] + DFT[\ln(I_{background})] \tag{10}$$

Then, feature processing in the frequency domain is completed through the filter as shown in (11):

$$H_1(u, v) = (\gamma_H - \gamma_L)\left[1 - e^{-c\left[\frac{D^2(u,v)}{D_0^2}\right]}\right] + \gamma_L \tag{11}$$

where, γ_H, γ_L control the amplitude range of the filter. c controls the filter morphology, and, it indicates the steepness (slope) of the transition section from low to high frequencies, and the larger its value, the steeper the slope band.

Then, image processing methods such as inverse Fourier transform and exponential transform are used to enhance the defect information, and weaken the fluctuation of the background.

Furtherly, according to the vertical relationship between the normal vector and all vectors on the tangent plane, the following equations can be obtained:

$$\begin{cases} N_z z(x+1, y) - N_z z(x, y) = -N_x \\ N_z z(x, y+1) - N_z z(x, y) = -N_y \end{cases} \tag{12}$$

Therefore, for the size of the image is $m \times n$, the sparse matrix $\boldsymbol{M}$ with the size of $(2 \times m \times n) \times (m \times n)$ can be obtained, and the vector $\boldsymbol{V}$ with the size of $(2 \times m \times n) \times 1$. For the whole image, (12) can be converted into:

$$\boldsymbol{MZ} = \boldsymbol{V} \tag{13}$$

where, $\boldsymbol{M}$ is made up of N_z, $\boldsymbol{V}$ is made up of N_x, N_y.

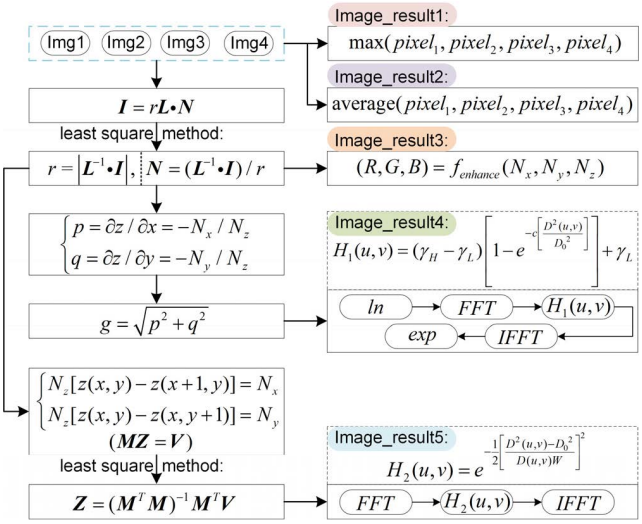

FIGURE 3. Algorithm flow chart of ZTSCI.

Then, the above overdetermined liner equations are solved by least square method of conjugate gradient method by making equation symmetric and positive definate.

$$\boldsymbol{Z} = (\boldsymbol{M}^{\boldsymbol{T}}\boldsymbol{M})^{-1}\boldsymbol{M}^{\boldsymbol{T}}\boldsymbol{V} \tag{14}$$

However, because actual situation does not accord with the theoretical hypothesis, there will be a large error in the reconstructed height feature. That is, the height calculated isn't the exact absolute height. For example, the height of plane will be inconsistent in the reconstruction result, and the defect characteristics will be covered up. However, there is a relatively accurate variation in relative height around the defect, obtained by the filter in (15):

$$H_2(u, v) = e^{-\frac{1}{2}\left[\frac{D^2(u,v) - D_0^2}{D(u,v)W}\right]^2} \tag{15}$$

Thus, the relative height variation around the defect is retained, and the fluctuation of background in height feature is reduced. At the same time, the surface texture with slow change in height feature is weakened.

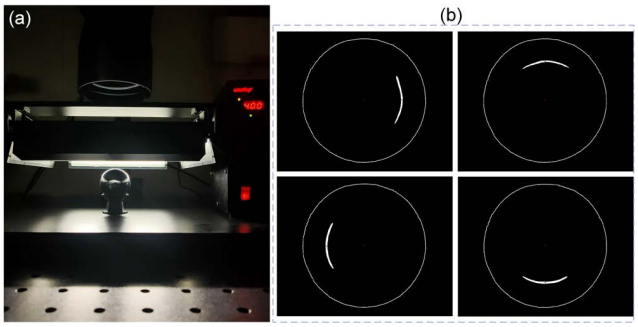

FIGURE 4. A four-zone and time-sharing exposure visual imaging system is built, and the calculation of incident lights is completed: (a) constructed system structure; (b) the calculation of incident lights.

The ZTSCI designed in this paper can calculate multiple feature images, such as the fusion images of maximum value and mean value, the color enhanced image of surface normal vector, the feature enhanced images of surface gradient and relative height. In addition, the calculation errors and surface fluctuation introduced by theoretical assumptions can be reduced through the above processing. So, it can avoid the interference on the characteristics of the defects. Furthermore, using different feature spaces, the difference between defect and interference information is enhanced. Therefore, in different features, the scratch defect on the surface can be distinguished from the non-defect with the same bright feature, and the pit defect can be distinguished from the foreign material with the same brightness variation. In this paper, the ZTSCI is mainly used to calculate multiple features of the surface to be detected, and to enhance the defect information in the image. The defect identification in the later stage is not described in this paper.

IV. EXPERIMENTS

According to the zonal and time-sharing computational imaging (ZTSCI) proposed in the paper, the visual imaging system is firstly built. The model of four-zone uniform strip light is C-HLM-170X25W-H-BY, which is equipped with PBL-12048-4 controller supporting successive stroboscopic brightening. In addition, the magnification ratio of telecentric lens is about $0.5\times$, the resolution of the camera is 5 million pixels, and the detection accuracy is about $20um$. And the Matlab R2016b is used to complete the calculation. The picture of the system built in this paper is shown in Fig. 4, in which four strip lights adopt low-angle lighting to form a high contrast between the bright features at the defect location and the dark features in the background.

The direction vectors of four incident lights in the system are solved by using a specular reflection ball. The reflection images of the incident lights passing through the surface of the ball are shown in (b). The calculated results are: $[0.9443, 0.0038, 0.3292]$, $[0.0009, 0.9563, 0.2922]$, $[-0.9435, -0.0247, 0.3305]$, $[-0.0021, -0.9451, 0.3268]$. Further, the visual imaging system shown in Fig. 4 is used to realize the imaging of the new energy battery.

Fig. 5 (a) is the imaging results under four groups of illumination. According to the images under different lights, and the direction matrix, photometric stereo is used to reconstruct the surface directly, as shown in Fig. 5(b). Because the application scenario cannot fully meet the theoretical assumptions, large height calculation error is generated, resulting in surface shape fluctuation of the plane. Therefore, the defects cannot be separated by the absolute value of height in (b). In addition, in order to facilitate later image processing, the reconstructed height map (b) is compressed into the gray range of $[0, 255]$, as shown in (c). It shows that the features at the defect location are covered by the surrounding background, making it impossible to carry out defect recognition. Based on the images under four groups of illumination, the ZTSCI proposed in this paper can be used to calculate the fused images and the color enhanced image of the normal vector, and can solve the problems of abnormal

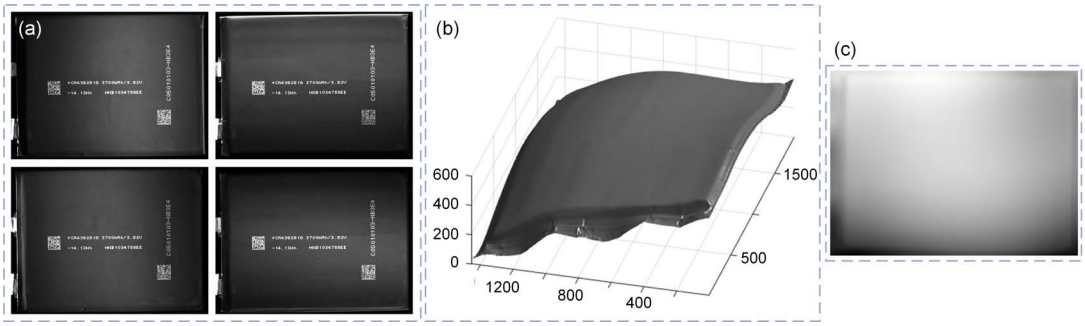

FIGURE 5. The results are directly processed by photometric stereo: (a) four groups of images are captured by the visual imaging system in this paper; (b) the reconstructed surface features; (c) the height map is compressed the gray range of [0,255].

gradient fluctuation and wrong height fluctuation, as shown in Fig. 6.

The processing results of ZTSCI are as shown in Fig. 6. According to gray images under different lighting conditions, the fusion images of maximum value and average value are calculated. Through these two groups of images, the gray distribution of the surface under traditional lighting conditions can be obtained. As can be seen from the figure, the defects of the surface are clearly preserved in the two-dimensional gray images. However, the inherent texture patterns existing on the surface, such as characters printed on the surface, are also preserved in the images. The information of texture has a high degree of similarity with the gray value of defects. And sometimes, the shape of printed characters will be similar to linear distribution of scratch defects or point-like distribution of pits and other information, so there will be a certain degree of false detection. In this paper, the normal vector of the surface is calculated according to the four groups of images and the direction vectors of incident lights. And the three-dimensional data of the normal vector is converted into a color image, so that the defect information which varies greatly in the normal vector feature can be easily distinguished by the color difference in the two-dimensional image. In addition, after calculating the gradient change image, the image processing such as filtering is used to obtain the enhanced image of gradient feature. On the one hand, it can overcome the gradient fluctuation in the surface shape caused by the calculation error mentioned above, and on the other hand, it can enhance the characteristics of gradient change at the defect location. As can be seen from the image of gradient change, the gradient characteristics of the plane are relatively consistent, showing bright gray characteristics in the boundary and defect with large gradient changes, thus facilitating subsequent defect identification. Furthermore, according to the surface normal vector distribution, the height distribution of the surface is solved by the least square method. Similarly, in order to avoid the fluctuation of height feature caused by calculation errors, the processing mentioned above is used to enhance the defect information with high variation frequency in height feature, and weaken the slowly changing surface fluctuation in height feature. Moreover, it can be found from the feature enhancement image of relative height that there will be a change of brightness for the boundary or defect location with a high frequency of feature change. That is, the area with lower relative height change is characterized by lower gray value, and the area with higher relative height change is characterized by higher gray value. Thus, in the later identification process, the defect can be directly segmented by using gray values, and the features with different height changes can be distinguished. From the enhanced images of surface normal vector, gradient feature, and relative height feature, it can be seen that the information distribution of the surface to be detected is relatively uniform and there is no excessive surface fluctuation as shown in Fig. 5. Furthermore, for the surface inherent texture such as (characters), since it has no height change, changing the direction of the incident light, will not result in the brightness changes around the texture. Thus, feature of texture will not be obtained in the results, avoiding excessive interference to the subsequent defect detection. The processing results of different defects in different features are shown in Fig. 7.

Firstly, the ZTSCI designed in this paper is used to fuse the maximum value and average value of the four groups of images under different incident lights. The results are similar to the gray images obtained by common machine visions. So, they are used in this article as comparison images for common vision methods. (a1) and (b2) are pit defects on the surface. Similar to the foreign material raised on the surface in (b1), they all have the characteristics of brightness variation. It can be seen from the three-dimensional representation diagrams of gray scale (a2), (b3) and (b4) that their gray intensity and morphology are also very similar. The above information cannot be separated by using the feature analysis only in gray space. In the enhanced images of normal vector, as shown in (a4), (b7) and (b8), the vector directions of the concave and convex shapes are different, and the color distribution around the corresponding positions in the figure is also different. That is, the left side of the pit has more red component, while the right side of the foreign material has more red component. In the enhanced images of gradient, as shown in (a5), (b9) and (b10), bright feature is near the edge of the target to be detected and dark feature is in the background.

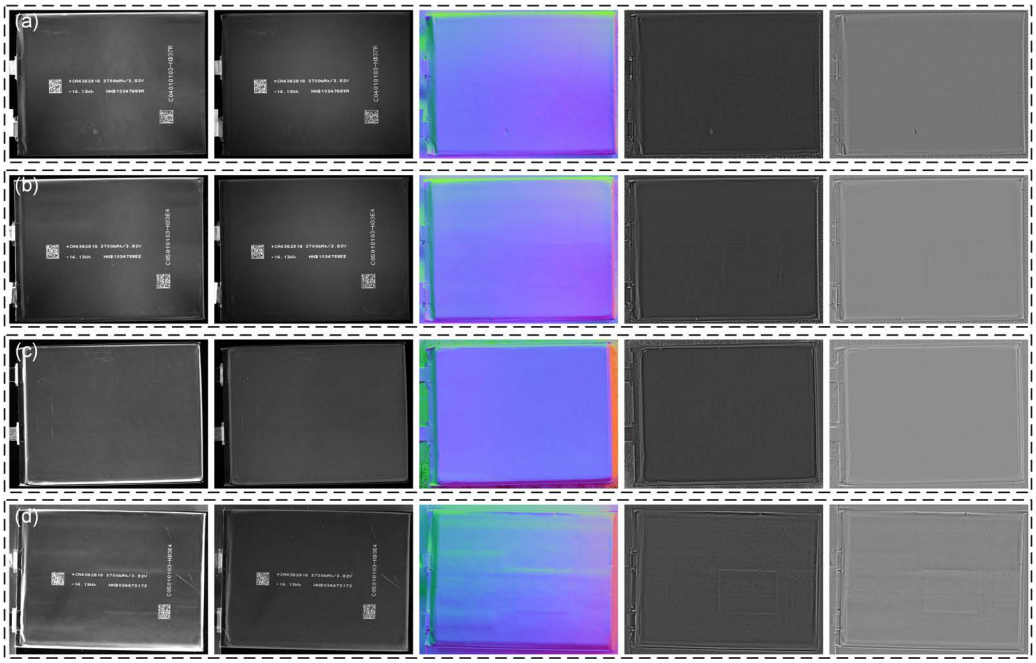

FIGURE 6. Processing results of ZTSCI, mainly including the images of maximum and average, enhanced images of normal vector, gradient and relative height: (a) the processing results of surface with pit defect; (b) the processing results of surface with raised foreign material; (c) the processing results of surface with bright lines or shallow marks (non-functional defects); (d) the processing results of surface with scratch defects.

In other words, only the information with gradient changes is preserved in the graph. In addition, the surface character texture in (a) and (b) has been transformed into a feature with lower gradient variation, which is similar to the black background. In the enhanced images of relative height, which has been compressed into the gray range of [0, 255], as shown in (a6), (b11) and (b12), since the height value of the pit defect is lower than that of its periphery, its relative height feature is shown as a lower gray value in the figure. By comparison, the foreign material raised on the surface has a larger height relative to the surrounding height. Therefore, its relative height feature shows a higher gray value in the figure. Moreover, in the three-dimensional representation diagram of relative height feature, as shown in (a7), (b13) and (b14), the pit defect and foreign material raised on the surface can be directly distinguished.

For different types of bright lines contained in (c) and (d), for example, (c1) is the surface bright line without damaging the functionality of product (can be called non-functional defect in this paper). Instead, they only destroy the surface coating. (d1) and (d2) are common scratch defects, which cause certain damage to the surface. However, both kinds of information are presented as bright lines in gray images. And, as can be seen from (c2), (d3) and (d4), the intensity difference of bright lines is small, so it is impossible to distinguish them directly according to grayscale characteristics. However, by using the method proposed in this paper, it can be seen from the figures of the calculated normal vector that the surface bright lines in (c4) of non-functional defect have no obvious characteristics, while the normal vector of the common scratch defects in (d7) and (d8) have obvious linear change. Furthermore, the enhanced images of gradient in (c5), (d9), and (d10), show that the gradient change of the former is similar to the surrounding background, while the gradient change of the latter is obviously different. In addition, it can be seen from the images of relative height in (c6), (d11), and (d12), that the height change of the former is relatively small. That is, its depth is very shallow, which will not cause functional damage to the surface. The height of the latter changes strongly, forming a strong contrast with the background. It can be seen from (c7), (d13) and (d14) that common scratches have obvious characteristics of depth variation, while non-functional bright lines have no depth change. So, different types of bright lines can be distinguished by using the different features mentioned above.

Above all, ZTSCI presented in this paper, firstly builds the four-zone and time-sharing exposure visual imaging system, and acquires shadow images in four lighting directions. Then, combined with the direction vectors of incident lights, different feature images are calculated, such as maximum fused image, average fused image, the enhanced images of normal vector, gradient and relative height. And it can avoid the large surface fluctuation error caused by theoretical hypothesis in practical application, which interferes with defect detection. Through the fusion of the maximum value and the average

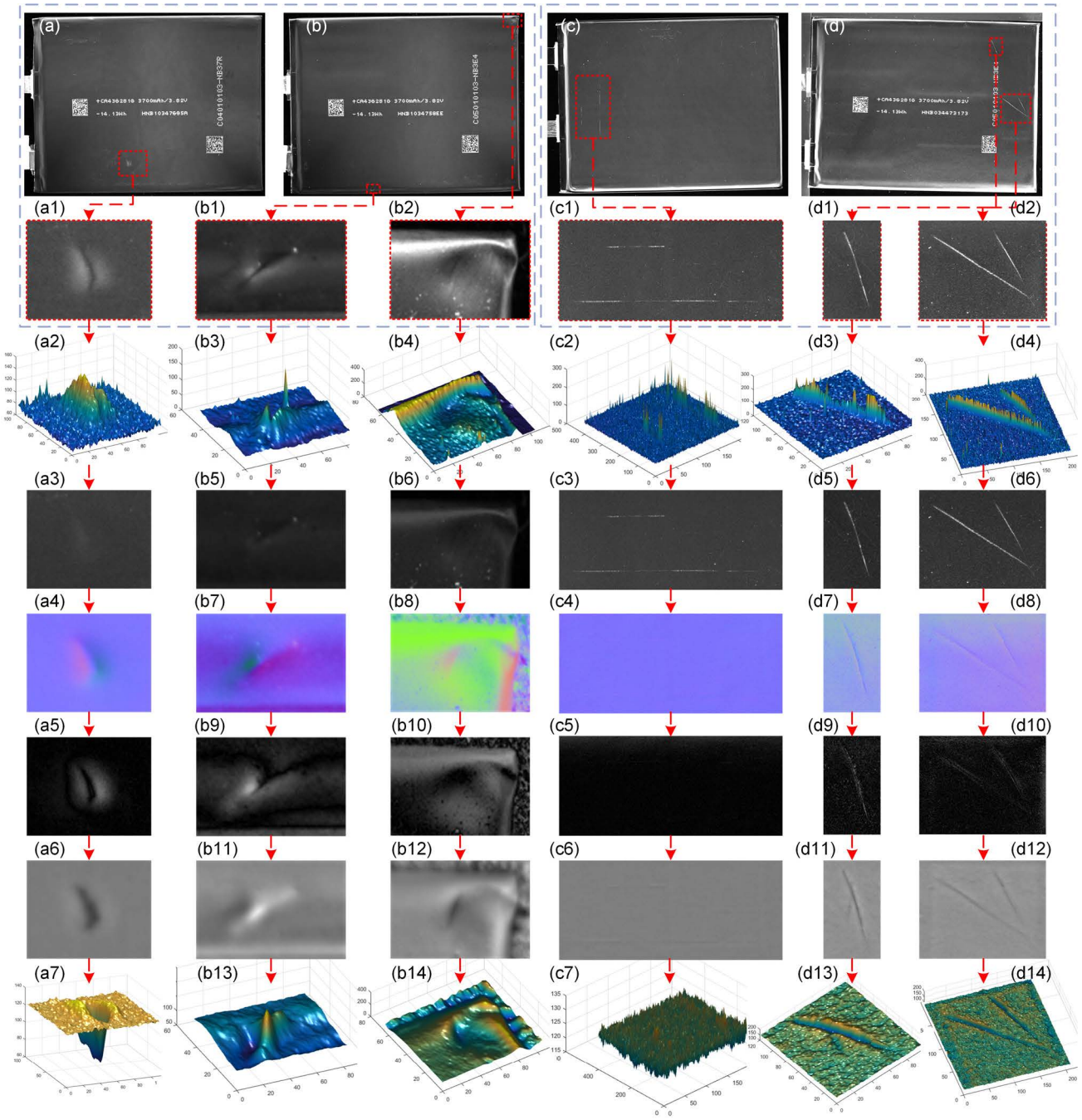

FIGURE 7. The processing results of different defects in different features, which mainly include the fusion results of maximum value and average value, three-dimensional representation diagrams of gray intensity, enhancement results of normal vector near the defects, enhancement results of gradient, enhancement results of relative height, and three-dimensional representation diagrams of the relative height feature: (a) the calculated results of features near pit defects; (b) the calculated results of features near raised foreign material and pit defect; (c) the calculated results of features near bright lines or shallow marks (non-functional defect); (d) the calculated results of features near scratch defects.

value, similar results can be obtained with common visual imaging. Although not directly from the image to distinguish the different information, such as pits and the foreign material raised on the surface have the same brightness variation, these information have a strong contrast with the surrounding background in the grayscale images. With this contrast, it can facilitate the segmentation of the above information from the large-area background directly, and reduce the calculation of

the subsequent recognition algorithm. In the enhanced image of normal vector, the normal vector changes of surface can be represented by the color differences between R, G and B, so that different features can be distinguished more obviously. In addition, in the image of gradient feature, the inherent surface texture features can be effectively weakened to avoid their interference to the detection. Furthermore, in the image of relative height, the concave and convex information of the surface can be represented as the features with lower gray scale and the features with higher gray scale respectively. And, the gray scale can be used to distinguish the target with different height changes. The ZTSCI proposed in this paper, on the one hand, can get the gray-scale characteristic information similar to the common machine vision methods, and on the other hand, it can get the different features at a lower cost, such as normal vector, gradient and relative height, thus enhancing the difference of easily-confused information in different feature spaces. Therefore, it lays a foundation for the segmentation and recognition of features in subsequent calculations.

V. CONCLUSION

In order to solve the misjudgment problem of different information in common gray images due to the very similar features such as morphology and gray value, and to avoid the high cost of using 3-D sensors in defect detection, a zonal and time-sharing computational imaging (ZTSCI) is proposed in this paper. Firstly, by monocular telecentric imaging and zonal light source, a four-zone and time-sharing exposure visual imaging system is constructed, thus reducing the cost of hardware. Then, according to the gray images under four groups of lighting conditions, and the direction vectors of incident lights, different feature images are calculated, such as maximum fused image, average fused image, the enhanced images of normal vector, gradient and relative height. On the one hand, the traditional gray images are obtained by image fusion can have a strong contrast, which can facilitate the segmentation of different information from the large-area background directly. On the other hand, it can enhance the separability of the target to be recognized in different feature spaces. Therefore, the suspected defects, which include different defects and easily-confused information, can be quickly segmented from the background in the traditional gray images, and the confusion of similar features in traditional gray image can be overcome by using multi-feature spaces. In addition, the ZTSCI is applied in the surface detection of new energy battery. In the gray image captured by common machine vision methods, the pit defects and the foreign material raised on the surface have similar brightness changes and similar morphological characteristics, and the bright lines of non-functional defects and common scratches on the surface also have similar grayscale characteristics. Through the calculation in this paper, the differences between the easily-confused information and defects can be enhanced in different feature spaces. Thus, it can reduce the difficulty of defects recognition and lay a foundation for improving the accuracy of recognition.

REFERENCES

[1] J. Jiang, P. Cao, Z. Lu, W. Lou, and Y. Yang, "Surface defect detection for mobile phone back glass based on symmetric convolutional neural network deep learning," *Appl. Sci.*, vol. 10, no. 10, p. 3621, May 2020.
[2] M. Yang, B. Zhang, J. Zhang, and H. Su, "Defect detection and classification for mobile phone cover glass based on visual perception," in *Proc. Chin. Control Decis. Conf. (CCDC)*, Aug. 2020, pp. 2530–2535.
[3] L. Jiang, Y. Wang, Z. Tang, Y. Miao, and S. Chen, "Casting defect detection in X-ray images using convolutional neural networks and attention-guided data augmentation," *Measurement*, vol. 170, Jan. 2021, Art. no. 108736.
[4] A. Choudhary, D. Goyal, and S. S. Letha, "Infrared thermography-based fault diagnosis of induction motor bearings using machine learning," *IEEE Sensors J.*, vol. 21, no. 2, pp. 1727–1734, Jan. 2021.
[5] L. Chen, Y. Yang, H. Chai, Y. Zhang, F. Wu, L. Zhou, K. Yan, J. Bai, Y. Shen, Q. Xu, and H. Jiang, "Dark-field detection method of shallow scratches on the super-smooth optical surface based on the technology of adaptive smoothing and morphological differencing," *Chin. Opt. Lett.*, vol. 15, no. 8, pp. 53–57, 2017.
[6] R. Zha, X. Jia, J. Li, and Z. Lian, "Optical fiber defects detection based on Gabor filter," in *Proc. IEEE Int. Conf. Prog. Informat. Comput. (PIC)*, Dec. 2020, pp. 168–172.
[7] L. Meiju, Z. Rui, G. Xifeng, and Z. Junrui, "Application of improved Otsu threshold segmentation algorithm in mobile phone screen defect detection," in *Proc. Chin. Control Decis. Conf. (CCDC)*, Aug. 2020, pp. 4919–4924.
[8] X. Fang, Q. Luo, B. Zhou, C. Li, and L. Tian, "Research progress of automated visual surface defect detection for industrial metal planar materials," *Sensors*, vol. 20, no. 18, p. 5136, Sep. 2020.
[9] Y. Zhang, Y. Zhang, and J. Gong, "A LCD screen Mura defect detection method based on machine vision," in *Proc. Chin. Control Decis. Conf. (CCDC)*, Aug. 2020, pp. 4618–4623.
[10] S. Fekri-Ershad and F. Tajeripour, "Multi-resolution and noise-resistant surface defect detection approach using new version of local binary patterns," *Appl. Artif. Intell.*, vol. 31, nos. 5–6, pp. 395–410, 2017.
[11] S. Fekri-Ershad and F. Tajeripour, "A robust approach for surface defect detection based on one dimensional local binary patterns," *Indian J. Sci. Technol.*, vol. 5, no. 8, pp. 3197–3203, Aug. 2012.
[12] T. Almeida, F. Moutinho, and J. P. Matos-Carvalho, "Fabric defect detection with deep learning and false negative reduction," *IEEE Access*, vol. 9, pp. 81936–81945, 2021.
[13] H.-I. Lin and F. S. Wibowo, "Image data assessment approach for deep learning-based metal surface defect-detection systems," *IEEE Access*, vol. 9, pp. 47621–47638, 2021.
[14] E. Westphal and H. Seitz, "A machine learning method for defect detection and visualization in selective laser sintering based on convolutional neural networks," *Additive Manuf.*, vol. 41, May 2021, Art. no. 101965.
[15] Y. Wu, X. Zhang, and F. Fang, "Automatic fabric defect detection using cascaded mixed feature pyramid with guided localization," *Sensors*, vol. 20, no. 3, p. 871, Feb. 2020.
[16] Q. Zhang, K. Barri, S. K. Babanajad, and A. H. Alavi, "Real-time detection of cracks on concrete bridge decks using deep learning in the frequency domain," *Engineering*, vol. 7, no. 12, pp. 1786–1796, Dec. 2021.
[17] L. Li, D. Liu, P. Cao, S. Xie, Y. Li, Y. Chen, and Y. Yang, "Automated discrimination between digs and dust particles on optical surfaces with dark-field scattering microscopy," *Appl. Opt.*, vol. 53, no. 23, pp. 40–5131, 2014.
[18] X. Tao, D. Xu, Z.-T. Zhang, F. Zhang, X.-L. Liu, and D.-P. Zhang, "Weak scratch detection and defect classification methods for a large-aperture optical element," *Opt. Commun.*, vol. 387, pp. 390–400, Mar. 2017.
[19] J. Ren and X. Huang, "Defect detection using combined deep autoencoder and classifier for small sample size," in *Proc. IEEE 6th Int. Conf. Control Sci. Syst. Eng. (ICCSSE)*, Jul. 2020, pp. 32–35.
[20] J. Zhang and G. Qiang, "Research on identification of dust particles on COF," in *Proc. MATEC Web Conf.*, vol. 61, 2016, p. 4018.
[21] Z. Xiong, Q. Li, Q. Mao, and Q. Zou, "A 3D laser profiling system for rail surface defect detection," *Sensors*, vol. 17, no. 8, p. 1791, Aug. 2017.

[22] S. Jiang, X. Li, and Y. Xing, "Repair method of data loss in weld surface defect detection based on light intensity and 3D geometry," *IEEE Access*, vol. 8, pp. 205814–205820, 2020.
[23] A. Sioma, "Automated control of surface defects on ceramic tiles using 3D image analysis," *Materials*, vol. 13, no. 5, p. 1250, Mar. 2020.
[24] R. Miao, Z. Shan, Q. Zhou, Y. Wu, L. Ge, J. Zhang, and H. Hu, "Real-time defect identification of narrow overlap welds and application based on convolutional neural networks," *J. Manuf. Syst.*, vol. 62, pp. 800–810, Jan. 2022.
[25] J. C. Stover and Y. A. Eremin, "Method for discriminating between holes in and particles on a film covering a substrate," U.S. Patent 6 486 946 B1, 2002.
[26] F. Wu, Y. Yang, J. Jiang, P. Zhang, Y. Li, X. Xiao, G. Feng, J. Bai, K. Wang, Q. Xu, and H. Jiang, "Classification between digs and dust particles on optical surfaces with acquisition and analysis of polarization characteristics," *Appl. Opt.*, vol. 58, no. 4, pp. 1073–1083, 2019.
[27] L. P. Zhao, L. Xiang, and Z. P. F. Ng, "TIR illumination technology for defect inspection of plastic ophthalmic lenses," *Opt. Precis. Eng.*, vol. 19, no. 9, pp. 2247–2254, 2011.
[28] K. Hu, "Defect detection based on contourlet-based shape from shading," *J. Mech. Eng.*, vol. 54, no. 6, p. 102, 2018.
[29] L. Yi, W. Xin, C. W. Swonger, and J. Ni, "Defect detection and classification of machined surfaces under multiple illuminant directions," *Proc. SPIE*, vol. 7798, Sep. 2010, Art. no. 77981T.
[30] D. Kang, Y. J. Jang, and S. Won, "Development of an inspection system for planar steel surface using multispectral photometric stereo," *Opt. Eng.*, vol. 52, no. 3, p. 9701, 2013.
[31] X. Huang, L. U. Hongjian, C. Ren, and C. Huang, "The method of aluminum foil defect detection in medicine packaging based on four-light photometric stereo method," *Packag. J.*, vol. 10, no. 3, pp. 47–51, 2018.
[32] G. Podrekar, D. Tomazevic, B. Likar, and P. Usenik, "Model based visual inspection of pharmaceutical tablets with photometric stereo," in *Proc. 15th IAPR Int. Conf. Mach. Vis. Appl. (MVA)*, May 2017, pp. 133–136.
[33] R. J. Woodham, "Photometric stereo: A reflectance map technique for determining surface orientation from image intensity," *Proc. SPIE*, vol. 155, pp. 136–143, Jan. 1978.
[34] L. Tsu-Yao, H. Wen-Hsing, and C. Yung-Sheng, "Shape description via shading images," *Image Vis. Comput.*, vol. 10, no. 1, pp. 46–54, Jan. 1992.